Icarus 296 (2017) 39–48

Contents lists available at ScienceDirect

Icarus

journal homepage: www.elsevier.com/locate/icarus

Solar wind scattering from the surface of Mercury: Lessons from the Moon

Charles Lue[a,b,c,*], Yoshifumi Futaana[a], Stas Barabash[a], Martin Wieser[a], Anil Bhardwaj[d,e], Peter Wurz[f], Kazushi Asamura[g]

[a] Swedish Institute of Space Physics, Box 812, SE-98128 Kiruna, Sweden
[b] Department of Physics, Umeå University, Linnaeus väg 24, SE-90187 Umeå, Sweden
[c] Department of Physics and Astronomy, University of Iowa, 30 N Dubuque St, IA 52242 Iowa City, United States
[d] Space Physics Laboratory, Vikram Sarabhai Space Center, Trivandrum 695 022, India
[e] Physical Research Laboratory, Ahmedabad 380009, India
[f] Physikalisches Institut, University of Bern, Sidlerstrasse 5, CH-3012 Bern, Switzerland
[g] Institute of Space and Astronautical Science, Japan Aerospace Exploration Agency, 3-1-1 Yoshinodai, Sagamihara 252-5210, Japan

ARTICLE INFO

Article history:
Received 6 September 2016
Revised 11 May 2017
Accepted 24 May 2017
Available online 25 May 2017

ABSTRACT

We discuss the surface-scattering of solar wind protons at Mercury based on observed scattering characteristics from lunar regolith. The properties of the impinging plasma are expected to be different between different regions on Mercury, and between Mercury and the Moon. Here, we review the expected Hermean plasma conditions and lunar empirical scattering models. We present observed and modeled energy spectra for scattered protons and hydrogen energetic neutral atoms (ENAs) for three cases of very different plasma conditions at the Moon. Then, we simulate scattering from the Hermean surface by applying the empirical models to four different scenarios of plasma precipitation on Mercury. The results suggest that surface-scattering is a strong source of ENAs at Mercury (up to $\sim 10^8\ \mathrm{cm^{-2}\,s^{-1}}$), which can be very useful for remote-sensing of the plasma conditions at the surface. Protons scattered from the surface back into space are also expected with high fluxes up to $\sim 10^7\ \mathrm{cm^{-2}\,s^{-1}}$, and may be important for wave generation and the filling in of the loss cone of mirroring and quasi-trapped populations. Scattered protons at the cusp region (of $\sim 10^6\ \mathrm{cm^{-2}\,s^{-1}}$) can potentially be detected by orbiters as outflowing protons within the loss cone.

1. Introduction

The planet Mercury has a global intrinsic magnetic field generated by an internal dynamo, like the Earth (e.g., Ness et al., 1975), but it has only a tenuous, surface-bounded exosphere, like the Moon (*e.g.*, Killen and Ip, 1999; Killen et al., 2007). This combination makes Mercury a unique obstacle to the solar wind. The magnetosphere modifies the global precipitation of plasma onto the Hermean regolith (e.g., Goldstein et al., 1981).

Precipitating plasma can cause emission of particles from the surface through sputtering of secondary particles originating from the surface (e.g., Johnson and Baragiola, 1991) or by scattering of the incident, primary particles (*e.g*,. Niehus et al., 1993). Over time, particle implantation and sputtering modifies the structure, elemental composition, and chemical state of the surface, including the formation of hydroxyl and water (*e.g.*, Pieters et al., 2009) and nanophase iron (*e.g.*, Hapke, 2001) on grain surfaces. The surface interactions also play an important role in the production of the exosphere and planetary plasma populations. See Milillo et al. (2005) for a review of this coupled system.

The particle emissions can also be diagnostic of the surface structure and composition (e.g., Johnson and Baragiola, 1991; Niehus et al., 1993; Grande, 1997) and of the precipitating plasma species, flux, and velocity (e.g., Grande, 1997; Wurz, 2000; Lukyanov et al., 2004; Futaana et al. (2006, 2013). Neutral particles that are emitted with velocities much larger than the planetary escape velocity (4 km/s for Mercury; 2 km/s for the Moon) can thus be studied by orbiters for remote investigation of the Hermean surface and plasma environment. These neutral particles with kinetic energies > 10 eV (*i.e.*, > 40 km/s in the case of hydrogen atoms) are called energetic neutral atoms (ENAs).

The potential for ENA observations at Mercury has been discussed (*e.g.*, Kazama et al., 2006; Orsini et al., 2010; Saito et al., 2010) in preparation for the upcoming Bepi-Colombo mission to Mercury. In those studies, emphasis was placed on sputtering

---

[*] Corresponding author.
E-mail address: charles.lue@irf.se (C. Lue).

http://dx.doi.org/10.1016/j.icarus.2017.05.019
0019-1035/© 2017 Elsevier Inc. All rights reserved.

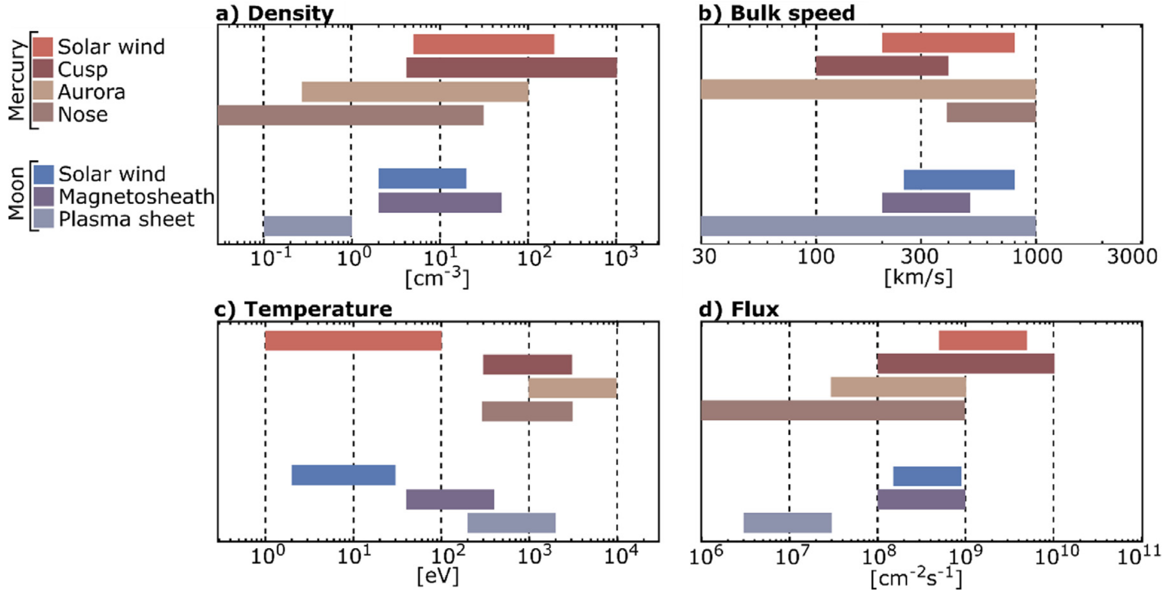

Fig. 1. Plasma parameters for the solar wind at the orbit of Mercury (0.31–0.46 AU) and at the orbit of the Earth (1 AU), and for the plasma at the most exposed regions of the Herman surface and lunar surface. The parameters shown are (a) ion density, (b) ion bulk speed, (c) ion temperature, and (d) ion flux. The parameter ranges are meant to represent both the model uncertainty and real variability. See Chapter 2 for more details.

and exospheric charge-exchange processes. However, lunar observations (McComas et al. 2009; Wieser et al., 2009) have shown that scattering is very effective (~10%–20% of the incident solar wind flux), and that the scattered particles dominate the ENA emissions.

A fraction of the particles scattered from a surface are charged. At the Moon, typically about 0.1%–1% of the solar wind flux is scattered as protons (Saito et al., 2008; Lue et al., 2014). These particles may be analyzed in a similar way as the scattered ENAs to learn about the surface and the plasma precipitation, although their trajectories away from the surface will be strongly controlled by the Hermean magnetosphere.

In the present study, we focus on scattered particles. Our purpose is to make predictions of the solar wind scattering at the Hermean regolith. In Section 2, we review the plasma environment near the Moon and Mercury. In Section 3, we present our chosen empirical models for solar wind scattering off regolith and compare the model predictions with a set of case studies from Chandrayaan-1 observations at the Moon. In Section 4, we apply the empirical models to conditions expected at different regions of the Hermean surface. In Section 5, we discuss the significance of scattered hydrogen as an ENA population at Mercury, and the significance of scattered protons in the Hermean magnetosphere.

2. Plasma precipitation onto Mercury and the Moon

The plasma conditions at Mercury and the Moon are different for several reasons. At Mercury's distance from the Sun, the solar wind is much denser, slightly slower (Parker, 1958), and hotter (Marsch et al., 1982) than at the Moon. Additionally, Mercury has a magnetosphere that strongly affects the properties of the precipitating plasma (e.g., Goldstein et al., 1981; Slavin et al., 2014). The Moon is also exposed to various plasma environments due to its orbit around the Earth, in which it passes the undisturbed solar wind as well as the magnetosheath and the magnetotail (*e.g.*, Frank, 1985). In this section, we review the properties of the solar wind at Hermean and lunar distances and the modifications that arise due to the Hermean and terrestrial magnetospheres. We summarize the results of the following review in Fig. 1.

2.1. Solar wind parameters at Mercury and the Moon

The solar wind parameters at Mercury's orbit (0.31–0.46 AU) have been studied by Sarantos et al. (2007, ff. 1,2). From their results, we see that the proton density is typically within $n = 5$–$200\,\mathrm{cm}^{-3}$ and the bulk speed $v = 200$–800 km/s. In the regular solar wind, the bulk speed and density variations are anticorrelated. We evaluate the corresponding flux to be within the range $J = 5{\cdot}10^{8}$–$5{\cdot}10^{9}\,\mathrm{cm}^{-2}\,\mathrm{s}^{-1}$. We can obtain an estimate for the corresponding plasma temperature range by using the empirical model by Lopez and Freeman (1986, c.f. Section 7 and Table 1) of the solar wind temperature as a function of the bulk speed and distance from the Sun. The result is a proton temperature in the range of $k_B T = 1$–100 eV. The model can be compared with WSA-ENLIL model results and MESSENGER observations presented by Baker et al. (2011, Figs 7 and 11), reporting an observed temperature of ~10 eV for a solar wind speed of ~300 km/s; ~20 eV for ~350 km/s; and ~40 eV for ~450 km/s. Corresponding ENLIL model results at the times were: ~4 eV; ~20 eV; and ~10 eV. The model by Lopez and Freeman (1986) returns similar values (using for simplicity the Hermean semi-major axis): $k_B T$(300 km/s, 0.39 AU) = 7 eV; $k_B T$(350 km/s, 0.39 AU) = 10 eV; and $k_B T$(450 km/s, 0.39 AU) = 20 eV.

Typical ranges for the solar wind parameters at 1 AU are: $n = 2$–$20\,\mathrm{cm}^{-2}$, $v = 250$–800 km/s, $k_B T = 2$–30 eV, and $J = 1.5$–$9{\cdot}10^{8}\,\mathrm{cm}^{-2}\,\mathrm{s}^{-1}$ (*e.g.*, Feldman et al., 1978; Katsavrias et al., 2012).

2.2. Plasma precipitation on the Moon

The plasma parameters listed above for undisturbed solar wind at 1 AU are applicable to the dayside of the Moon when it is outside of the terrestrial magnetospheric regions. The small solar wind proton thermal speed relative to the bulk speed results in an incident flux onto the surface that decreases approximately as cosine of the solar-zenith angle (*SZA*).

Reflected protons from the terrestrial bow shock form an additional population in the foreshock region (Asbridge et al., 1968). Picked up by the interplanetary magnetic field, these reflected protons can reach up to three times the original solar wind speed.

However, they contribute by a few percent or less to the solar wind flux in the foreshock region and are not included in Fig. 1.

In the magnetosheath, the solar wind is heated ($k_BT = 40$–400 eV), decelerated ($v = 200$–500 km/s), and compressed ($n = 2$–50 cm^{-2}) (Frank, 1985). Because of the higher thermal spread in the magnetosheath, the precipitation onto the Moon is widened from the cosine *SZA* dependence.

In the magnetotail lobes, the plasma is very tenuous (∼0.01 cm^{-3}, not shown in Fig. 1). In the plasma sheet of the terrestrial magnetotail, the plasma has a very high temperature ($n = 0.1$–1 cm^{-3}; $v_b = 10$–1000 km/s; $k_BT = 200$–2000 eV) (Frank, 1985), effectively impacting the whole Moon due to the large thermal spread.

See also Lue et al. (2016a) for further discussion on the change of the incident plasma distribution on the Moon in the magnetosheath and plasma sheet.

Lunar magnetic anomalies can also modify the plasma precipitation locally (10–1000 km scale regions), but these effects (heating, deceleration, voids and reflection (e.g., Wieser et al., 2010; Lue et al., 2011; Saito et al., 2012; Vorburger et al., 2012, 2013; Poppe et al., 2014) are similar to those generated by the terrestrial environment, so we do not include the magnetic anomalies explicitly in Fig. 1.

2.3. Plasma precipitation on Mercury

Different paths of precipitation onto the surface of Mercury have been discussed in literature. The precipitation paths can be generally sorted into four categories (e.g., Goldstein et al., 1981): precipitation along (1) dayside open field lines; (2) closed field lines connected to the plasma sheet; (3) dayside closed field lines; and (4) the occasional direct precipitation when high solar wind pressure pushes the magnetopause below the Hermean surface. Here, we will refer to these types as (1) cusp; (2) aurora; (3) nose; and (4) direct precipitation, following the terminology used by Kallio and Janhunen (2003). Below, we will assign values of the plasma parameters for these precipitation classes and the corresponding surface regions, by reviewing results from theoretical models and computer simulations. In Fig. 1, we plot the ranges of values found through this review or, if not directly available, extrapolated values based on arguments made below. See also Killen et al. (2007, Section 3.5, Table 8) and Raines et al. (2013, 2015) for further review of the plasma precipitation on Mercury. It is worth noting that observations by the MESSENGER spacecraft have revealed that flux transfer events (FTEs) play a major role in the injection of plasma across the Hermean magnetopause (e.g., Slavin et al. (2009); Imber et al., 2014; DiBraccio et al., 2015; Sun et al., 2016), an effect that may be underestimated in early models.

2.3.1. Cusp precipitation

At the cusps of the Hermean magnetosphere, plasma can precipitate along open field lines. Here, the plasma is expected to be decelerated, compressed, and heated. Goldstein et al. (1981) assumed a deceleration of ∼250 km/s and an increase in density by a factor of four, out of which one-fifth ends up precipitating, giving a precipitating flux of $\sim 6{\cdot}10^8\ \mathrm{cm}^{-2}\ \mathrm{s}^{-1}$ (assuming an upstream $v_b = 400$ km/s, $n = 44\ \mathrm{cm}^{-3}$).

Qualitatively similar results were obtained in simulations by Massetti et al. (2003). Where the plasma entered the cusp, they observed a compression to twice the upstream density and deceleration to half the upstream speed, with a heating to thrice the upstream temperature. However, the properties upon precipitation varied significantly between different sub-regions of the cusp: the low-latitude boundary layer (LLBL), the cusp proper, and the mantle. The peak precipitation was found at the LLBL, where the plasma had been accelerated compared to the upstream speed, while the plasma was decelerated in the other regions. The mean precipitating fluxes in the cusp region was $\sim 4{\cdot}10^8\ \mathrm{cm}^{-2}\ \mathrm{s}^{-1}$ for nominal solar wind conditions ($v_b = 430$ km/s, $n = 200\ \mathrm{cm}^{-3}$).

Similar results were also obtained in hybrid simulations by Kallio and Janhunen (2003), resolving finite-gyro radius effects. For upstream values of $v_b = 430$ km/s, $n = 76\ \mathrm{cm}^{-3}$, $B_{IMF} = 10$–40 nT, they calculated ‘cusp’ precipitation of $\sim 10^8\ \mathrm{cm}^{-2}\ \mathrm{s}^{-1}$. In the extreme case of $v_b = 860$ km/s, the precipitation increased to $\sim 10^9\ \mathrm{cm}^{-2}\ \mathrm{s}^{-1}$. Likely because of the finite gyro radius of the precipitating protons, they mostly impacted the surface at closed field-line regions. Nevertheless, we consider it cusp precipitation here.

Mura et al. (2005) also simulated proton trajectories in the Hermean magnetosphere. They separated their results into decelerated protons (0.1–1 keV) and accelerated protons (1–10 keV). From the spatial distribution of the precipitation, we consider the former group representative of cusp-type precipitation and the latter of auroral type. The cusp-type precipitation was again at similar fluxes as in the other studies ($\sim 10^7$–10^8), with a peak of $3{\cdot}10^8\ \mathrm{cm}^{-2}\ \mathrm{s}^{-1}$. Sarantos et al. (2007), however, reported higher fluxes of $3{\cdot}10^9\ \mathrm{cm}^{-2}\ \mathrm{s}^{-1}$ at aphelion solar wind conditions, and roughly twice that for perihelion.

Particle observations by the MESSENGER spacecraft inside the Hermean cusps (Raines et al., 2014, Fig. 6), at 300–600 km altitude, show directional proton fluxes on the order of $3{\cdot}10^6\ \mathrm{cm}^{-2}\ \mathrm{sr}^{-1}\ \mathrm{s}^{-1}$, over a wide directional distribution and temperatures of 5.75 MK (500 eV). These fluxes ($\sim 3{\cdot}10^6\ \mathrm{cm}^{-2}\ \mathrm{s}^{-1}$) are relatively low compared to the aforementioned estimates. On the other hand, Poh et al. (2016) used MESSENGER magnetic field data to investigate the precipitation of protons through cusp filaments, and estimated a precipitation rate of $3{\cdot}10^{25}\ \mathrm{s}^{-1}$ in an area of $\sim 10^6\ \mathrm{km}^2$, giving an average precipitating flux of $\sim 3{\cdot}10^9\ \mathrm{cm}^{-2}\ \mathrm{s}^{-1}$.

In summary of these studies, we find peak flux estimates at the Hermean cusps ranging from $\sim 10^8$ to $10^{10}\ \mathrm{cm}^{-2}\ \mathrm{s}^{-1}$, even for a nominal solar wind assumption. This wide range is due to the uncertainty in modeling and observations but also differences in the definition of the precipitation area. We allow this range to also represent the smaller variability of the solar wind flow. The population that we consider to be cusp-precipitating is decelerated roughly to half the initial speed according to Goldstein et al. (1981) and Masetti et al. (2003). Considering a solar wind speed of 200–800 km/s (Sarantos et al., 2007), the cusp bulk speed would be ∼100–400 km/s. Note that individual particle speeds will generally be larger than the bulk velocity. Assuming that the loss of bulk energy is compensated by heating, the plasma would reach a temperature of ∼300–3000 eV. These properties combined suggest a density of in the range of ~ 3–$1000\ \mathrm{cm}^{-3}$.

2.3.2. Auroral precipitation

Goldstein et al. (1981) estimated that the precipitation of plasma via the plasma sheet was the dominant type of plasma precipitation at Mercury. This precipitation would occur over large auroral ovals, corresponding to a surface area of $\sim 2{\cdot}10^6\ \mathrm{km}^2$, with a mean precipitating flux in the auroral oval of $\sim 4{\cdot}10^7\ \mathrm{cm}^{-2}\ \mathrm{s}^{-1}$, and a plasma temperature of 7.5 keV.

The hybrid simulations by Kallio and Janhunen (2003) shows auroral precipitation of $\sim 3{\cdot}10^7\ \mathrm{cm}^{-2}\ \mathrm{s}^{-1}$. Peak values may reach $\sim 10^8\ \mathrm{cm}^{-2}\ \mathrm{s}^{-1}$, but it is difficult to clearly distinguish between ‘cusp’ and ‘aurora’ precipitation in the simulation results (Kallio and Janhunen, 2003; Fig. 3).

The aurora-like 1–10 keV protons precipitating according to the model by Mura et al. (2005) reached up to $10^9\ \mathrm{cm}^{-2}\ \mathrm{s}^{-1}$, although a clear distinction between cusp- and auroral precipitation was not made.

MESSENGER observations in the plasma sheet show densities of ~1–10 cm^{-3}, and temperatures of ~1–30 MK (~100–3000 eV) (Sun et al., 2016).

In summary, the auroral precipitation estimates range between $3{\cdot}10^7$ and 10^9 similar to lunar values, but the (thermal) energy of these protons (1–10 keV) is higher than the typical solar wind bulk energy. Because of the high temperature, the bulk speed is less important. Nevertheless, there should be a net flow down into the auroral regions. Using the terrestrial plasma sheet (Frank, 1985) as a reference, the bulk speed is likely within the range of 10–1000 km/s. The densities required to fulfill these parameters are ~0.3–100 cm^{-2}.

2.3.3. Nose precipitation

The non-negligible proton gyro radius compared to the Hermean dayside magnetosphere allows solar wind protons of sufficient energy to reach the surface even at regions of closed field-lines on the Hermean dayside. Goldstein et al. (1981) estimated that this precipitation amounts to a flux of ~10% of the auroral precipitation (or ~1% of the upstream solar wind).

Kallio and Janhunen (2003), with a model that resolves the proton gyro motion, similarly found that ~1% of the solar wind reached the subsolar “nose” region, for nominal solar wind conditions of $n = 76\ cm^{-3}$ and $v_b = 430$ km/s. They further found that an increase of the solar wind speed to twice the nominal value was sufficient to increase the nose precipitation to ~10% of the solar wind flux. However, we cannot clearly distinguish between the nose precipitation and cusp precipitation as we previously noted that the kinetic effects cause much of the cusp-precipitation to occur on closed field lines. In fact, we may look at the nose precipitation as the diffuse cusp experienced by the more energetic protons.

The plasma at the dayside magnetopause was studied using MESSENGER observations, by Gershman et al. (2013). Directional fluxes on the order of $10^6\ cm^{-2}\ sr^{-1}\ s^{-1}$ are observed in non-ideal (non-solar wind) viewing directions, suggesting that the flux through the magnetopause may be higher than $10^6\ cm^{-2}\ s^{-1}$, with a significant contribution from particles in the 1–10 keV energy range. Note that in the observed magnetic field of ~200 nT, the gyro radius for these protons is 20–60 km, while the magnetopause distance is ~1000 km. Thus, these protons travel along the closed field-lines over many gyrations before they impact the surface (*c.f.* Leblanc et al., 2003, Fig. 3).

We assume fluxes of ~0.1%–10% of the solar wind depending on the solar wind speed variations, corresponding to ~10^6–$10^9\ cm^{-2}\ s^{-1}$. Like the cusp population, the nose population would have experienced deceleration and heating at the bow shock. However, the precipitating nose component should come from the high-speed tail of this incident distribution. Thus, we expect a higher bulk speed than the cusp population. We assume a bulk speed of ~400–1000 km/s, and a temperature similar to the cusp population at ~300–3000 eV. Corresponding densities are ~0.03–30 cm^{-3}.

2.3.4. Direct precipitation

A clearly different type of precipitation occurs if the magnetopause is pushed below the Hermean surface, so that the solar wind impacts the surface undisturbed. Using magnetohydrodynamic simulations, Kabin et al. (2000) estimated the solar wind parameters required to push the magnetopause below the surface. They found that an increase in speed by a factor of 2.5 from the assumed nominal values of $n = 73\ cm^{-2}$, $v_b = 430$ km/s was sufficient to create such a situation (*i.e.*, a dynamic pressure of 70 nPa). They also noted that an increase in density by a factor 9 may achieve the same. These parameter values are very rare (*c.f.* Sarantos et al., 2007) but not impossible, as illustrated by one of the lunar cases presented herein where the solar wind pressure increased more than 10 times. Slavin et al. (2014) studied several extreme events with up to 65 nPa solar wind dynamic pressure at Mercury, and inferred from their observations a corresponding mean magnetopause standoff distance as low as 1.03 Mercury radii. Considering the north-south asymmetry of the Hermean magnetic field (Anderson et al., 2011), this implies that the magnetopause may have been suppressed below the Hermean surface over parts of the southern hemisphere (Slavin et al., 2014, Fig. 18).

3. Lunar empirical scattering models

Solar wind scattering from the lunar regolith has been studied for a range of different incident plasma parameters. The set of empirical models resulting from these studies allow us to predict scattered ENA and ion distributions at the Moon. However, the plasma parameters in the Hermean environment reviewed in the previous section show that the expected plasma at Mercury is sometimes beyond the ranges from which the empirical models have been derived.

In this section, we introduce and specify the empirical models and their implementation, and then show a set of lunar cases found at the edges of the parameter spaces that the empirical models were derived from.

3.1. Model description

We model scattered differential fluxes of hydrogen ENAs and protons in three steps: First, we calculate the total scattered flux J_{outENA} and J_{out+}, respectively (in the unit of $cm^{-2}\ s^{-1}$). Then, we calculate the directional flux j_{dENA}; j_{d+} ($cm^{-2}\ s^{-1}\ sr^{-1}$) in the direction toward the spacecraft location. Finally, we calculate the energy spectrum of differential flux j_{deENA}; j_{de+}($cm^{-2}\ s^{-1}\ sr^{-1}\ eV^{-1}$).

The total scattered flux is calculated by multiplying the incident proton flux J_{in} onto the surface with the expected scattering rate. Estimates of the ENA scattering rate from the lunar regolith range between ~10% and ~20% (*c.f.* Vorburger et al., 2013, Table 1). Dependencies on the bulk speed (Funsten et al., 2013) and temperature (Allegrini et al., 2013) of the incident plasma have been reported. On the other hand, other studies (Futaana et al., 2012; Lue et al., 2016a) found no strong dependence on these parameters. For the purposes of the present study, where we are interested in order-of-magnitude results, we simply assume a constant scattering rate of 20% for the hydrogen ENAs.

$$J_{outENA} = 0.2\ J_{in} \tag{1}$$

The proton scattering rate has been estimated to 0.1%–1% by Saito et al. (2008), or 0.01%–1% by Lue et al. (2014), where the latter study reported a strong correlation with the solar wind speed. For the present study, we use the empirical model from Lue et al. (2014) for proton scattering rate as a function of solar wind speed.

$$J_{out+} = 2.5\ \exp\left(\frac{-2500\ km/s}{v_{sw}}\right) J_{in} \tag{2}$$

To derive the directional flux, we used the empirical ENA scattering function that was developed by Schaufelberger et al. (2011), and updated by Vorburger et al. (2013). This scattering function describes the directional distribution, in elevation and azimuth, of hydrogen ENAs from the lunar regolith, as a function of the incidence angle of the solar wind. We assume the same directional scattering function for scattered protons. Note that we use the term plasma-zenith angle (*PZA*) rather than *SZA* to express the incidence angle because the plasma does not necessarily impact from the solar direction.

$$j_d = J_{out}\, f_s(az, el, PZA), \tag{3}$$

Table 1
Plasma parameters for selected lunar cases and simulated Hermean cases.

Case	Density	Bulk speed	Temperature	Incidence angle	Incident flux
I	140 cm^{-3}	260 km/s	0.92 eV	20°	$4{\cdot}10^9\ cm^{-2}\ s^{-1}$
II	4.6 cm^{-3}	550 km/s	21 eV	22°	$3{\cdot}10^8\ cm^{-2}\ s^{-1}$
III	1.6 cm^{-3}	220 km/s	130 eV	46°	$3{\cdot}10^7\ cm^{-2}\ s^{-1}$
Cusp	10 cm^{-3}	200 km/s	10^3 eV	10°	$2{\cdot}10^8\ cm^{-2}\ s^{-1}$
Aurora	1 cm^{-3}	200 km/s	10^4 eV	10°	$4{\cdot}10^7\ cm^{-2}\ s^{-1}$
Nose	1 cm^{-3}	600 km/s	10^3 eV	80°	$2{\cdot}10^7\ cm^{-2}\ s^{-1}$
Direct	10^3 cm^{-3}	400 km/s	10 eV	10°	$4{\cdot}10^{10}\ cm^{-2}\ s^{-1}$

where f_s is given by Vorburger et al. (2013, Appendix), and the division by cos(*PZA*) added for normalization to unity ($\int_0^{pi/2}\int_0^{2pi} f_s\ daz\ del = 1$).

To derive the differential flux of ENAs, we apply the empirical model for the energy spectrum from Futaana et al. (2012). A different model is presented by Rodríguez et al. (2012), but the differences are small.

$$j_{deENA} = j_{dENA} f_{EENA}(E; v_{sw}), \tag{4}$$

where f_E, adapted from Futaana et al. (2012) for normalization to unity ($\int_0^\infty f_{EENA} dE = 1$) is given by

$$f_{EENA} = \frac{E}{kT_{ENA}^2(v_{in})} \exp\left(-\frac{E}{kT_{ENA}(v_{in})}\right), \tag{5}$$

where kT_{ENA} is a function of the solar wind impact speed v_{in}.

$$kT_{ENA} = v_{in} \cdot 0.273\ eV\ s\ km^{-1} - 1.99\ eV. \tag{6}$$

For the proton scattering, we use the model from Lue et al. (2014), which multiplies the ENA spectrum with a probability to exit the surface with a positive charge, as a function of the exit speed.

$$j_{de+} = j_{d+} f_{E+}(E; v_{in}), \tag{7}$$

$$f_{E+} = f_{EENA}(E; v_{in}) \cdot \exp\left(\frac{-5000\,km/s}{v_+}\right) \Big/ \int_0^\infty f_{EENA} \cdot \exp\left(\frac{-5000\,km/s}{v_+}\right) dE, \tag{8}$$

where the denominator is added for normalization to unity ($\int_0^\infty f_{E+} dE = 1$), and $v_p = (2E/m_p)^{0.5}$, where m_p is the proton mass.

These empirical models can be directly applied to the nominal solar wind, where the incident beam is almost monodirectional and mono-energetic. However, to account for a significant plasma temperature, we need to integrate the above models (where v_{in} and *PZA* are functions of the incident velocity) over the velocity distribution function of the incident plasma. See Lue et al. (2016a) for a detailed description of this procedure. For the distribution functions used herein, we apply a kappa distribution with $\kappa = 2$, assuming a similarity to the terrestrial magnetosheath plasma (*e.g.*, Formisano et al., 1973).

3.2. Lunar case studies

The models used herein have been derived from observations by the Sub-keV Atom Reflecting Analyzer (SARA) (Barabash et al., 2009) on the lunar orbiter Chandrayaan-1. Here, we perform three case studies to illustrate the changes of the scattering with plasma parameters, according to the model results along with the spacecraft observations, for three very different plasma conditions.

Chandrayaan-1 had a polar lunar orbit at 100 km altitude, raised to 200 km in May 2009. SARA included two particle sensors: the Chandrayaan-1 Energetic Neutrals Analyzer (CENA) (Kazama et al., 2006) and the Solar Wind Monitor (SWIM) (McCann et al., 2007), measuring ENAs and ions respectively. The data used in this study are all from June 2009, during which Chandrayaan-1 was in a noon-midnight orbit (*c.f.* Lue et al., 2014, 2016a). The noon-midnight orbit is favorable for detection and distinction of surface-scattered protons from other proton populations and noise sources (Lue et al., 2014).

For the following case studies, we integrate measurements from CENA and SWIM over 20 minutes around the dayside equator crossing of Chandrayaan-1. For CENA, we subtract an estimated noise contribution of $0.3\cos^2(\text{SZA})$ counts per energy-direction bin per minute (Lue et al., 2016a). For SWIM, we subtract a constant background of 0.08 counts per energy-direction bin per minute and a solar wind cross-talk contribution of 10^{-4} of the solar wind signal, affecting energy bins just above the solar wind energy (Lue et al., 2014).

To monitor the solar wind conditions, we used data from the Solar Wind Experiment (SWE) (Ogilvie et al., 1995) on the Wind spacecraft at the Earth-Sun L1 point. The Wind/SWE solar wind data was time-shifted to account for the solar wind travel time from Wind to the Moon. For the case when the Moon is in the terrestrial magnetosheath, we instead use ion data from the Magnetic Field and Plasma Experiment-Plasma Energy Angle and Composition Explorer (MAP-PACE) instrument (Saito et al., 2010) on the Kaguya lunar orbiter, located in a very similar polar orbit to that of Chandrayaan-1. At the chosen period, both Kaguya and Chandrayaan-1 were located outside of the lunar wake (c.f. Lue et al., 2016a, ff. 2b, 4 g).

We look at the modeled energy spectra of reflected particles for three different cases in Fig. 2. The corresponding time periods (UT) for these cases are 2009-06-24 05:19–05:39; 2009–06–29 10:42–11:02; and 2009-06-05 04:20–04:40, respectively. These cases represent very different plasma conditions at the Moon, see Table 1.

In Fig. 2, we see that the models reasonably well reproduce the observed spectral shapes. The quantitative estimates exhibit deviations from the models, especially for the proton component. These deviations are small in the context of this study, but will be discussed further in Section 5.

4. Simulated solar wind scattering from the surface of Mercury

In this section, we apply the empirical scattering models presented in Section 3 to the expected Hermean plasma conditions presented in Section 2. We show simulated spectra for scattered hydrogen ENAs and protons from the Hermean regolith for four chosen plasma conditions, corresponding to cusp-, auroral-, nose-, and direct precipitation respectively. Although each case allows a wide range of possible parameters (see Fig. 1), we here choose parameters from within those ranges such that the cases are representative but also clearly different from each other (see Table 1). The calculated ENA and ion spectra are seen in Fig. 3. For all these cases, we employed the modified empirical models that allow for a large plasma temperature (see Section 3.1; Lue et al., (2016a)).

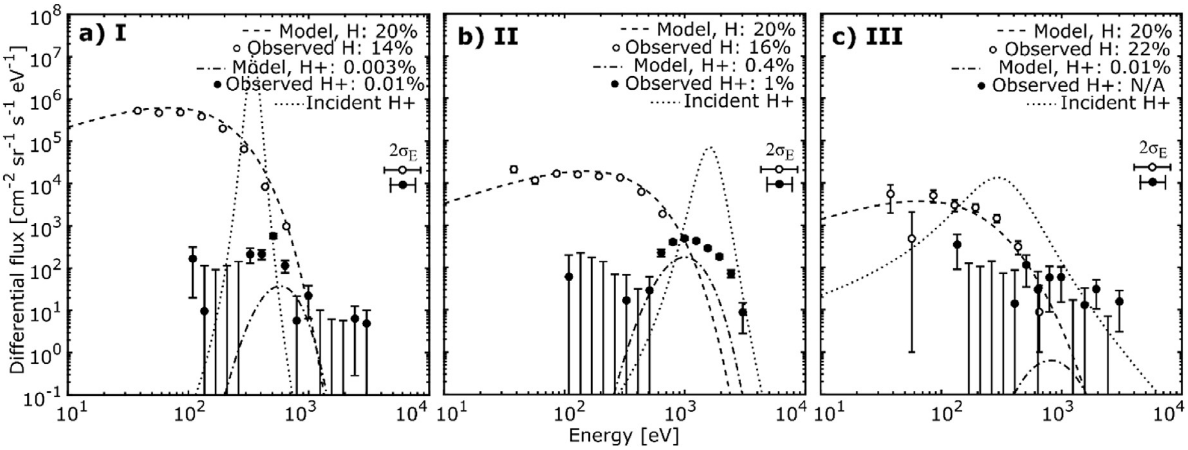

Fig. 2. Modeled and observed energy spectra of scattered proton and hydrogen distributions at the Moon, for cases I (a), II (b), and III (c). Vertical error bars indicate 1σ errors from count-rate statistics, and horizontal error bars (2σ_E) indicate the energy resolution of the CENA and SWIM sensors. The dotted lines indicate for reference the shape of the incident proton spectra, modeled as κ-distributions with the parameters listed in Table 1 and $\kappa = 2$. The magnitude of the reference incident spectrum is normalized to 5 times the ENA model for easier comparison.

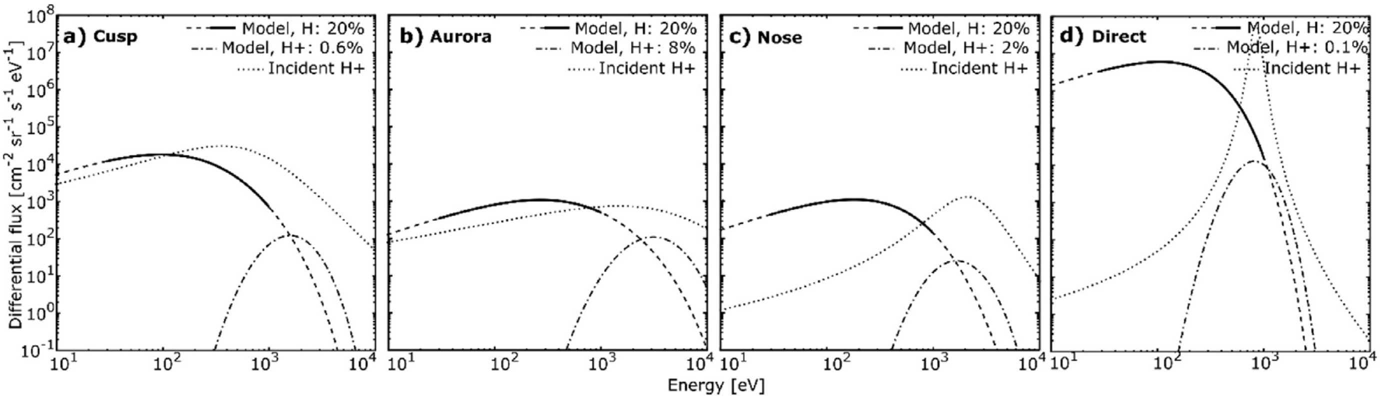

Fig. 3. Modeled energy spectra for hydrogen ENAs and protons, for (a) cusp precipitation, (b) aurora-like precipitation, (c) nose precipitation, and (d) direct precipitation during extreme solar wind pressure. The dotted lines represent the incident proton spectra for kappa distributions with the plasma parameters listed in Table 1 and $\kappa = 2$. The magnitude of the reference incident spectrum is normalized to 5 times the ENA model for easier comparison. The solid line indicates the best confined energy range of the ENA model from Futaana et al. (2012).

Because we are investigating the directional differential flux, we must choose a scattering direction. Here, we choose a direction close to zenith (azimuth: 10°, elevation 80°). This is an arbitrary choice but the results are not very sensitive to the chosen direction because the scattering function is close to isotropic for small PZAs or large plasma temperatures. Similarly, we must also select the incidence angle (PZA) (of the bulk plasma flow) for the models. We follow assumption that the magnetosphere of Mercury directs the plasma into small incidence angles (chosen PZA: 10°), except for the nose precipitation case, where the ions are suggested to be gyrating in the equatorial magnetic field of Mercury on trajectories that barely intersect the surface (chosen PZA: 80°).

Fig. 3a shows the energy spectra of scattered hydrogen ENAs and protons expected from the cusp region (or 'cusp proper', as denoted in Section 2.3.1); the footprint of the open-field line region of the dayside magnetosphere. As seen in Table 1 and Fig. 1, the plasma density ($n = 10\,\mathrm{cm}^{-3}$), bulk speed ($v_b = 200\,\mathrm{km/s}$), and flux, are within the ranges of the nominal solar wind, but the expected temperature is high ($k_BT = 1000\,\mathrm{eV}$). The low bulk speed is compensated by the high temperature, giving a proton reflection rate of ~0.6%.

Fig. 3b shows the predicted energy spectra of ENAs and protons from the auroral precipitation regions. The precipitating protons, arriving from the plasma sheet, have a very high temperature ($k_BT = 7\,\mathrm{keV}$). As a result, many protons impact with very high speed, increasing the expected proton reflection rate up to ~8%.

Fig. 3c shows the energy spectra of ENAs and protons expected in the subsolar region, due to nose precipitation, at the footprint of the dayside closed magnetic field line region of the magnetosphere. These precipitating protons have a high bulk speed ($v_B = 600\,\mathrm{km/s}$), and we get the proton scattering rate to be ~2%.

Fig. 3d shows the predicted energy spectra of ENAs and protons for the case of direct precipitation, when the solar wind pressure is sufficient to suppress the Hermean magnetopause below the surface. Because of the high flux (approximately 10 times more than the nominal solar wind at Mercury, and 100 times more than the typical precipitation onto the surface when the magnetosphere is not compressed), we also get a high flux of scattered particles. The low impact speed used for this example gives a proton scattering rate of 0.1%. The choice of high density or high velocity to represent this high dynamic pressure case is arbitrary, but we chose the high-density case for a clearer distinction to the other cases.

5. Discussion and implications

Comparing the expected proton precipitation in the Hermean environment with that in the lunar environment, the Hermean protons tend to have higher impact speeds due to the higher plasma temperature. The high plasma temperature also necessi-

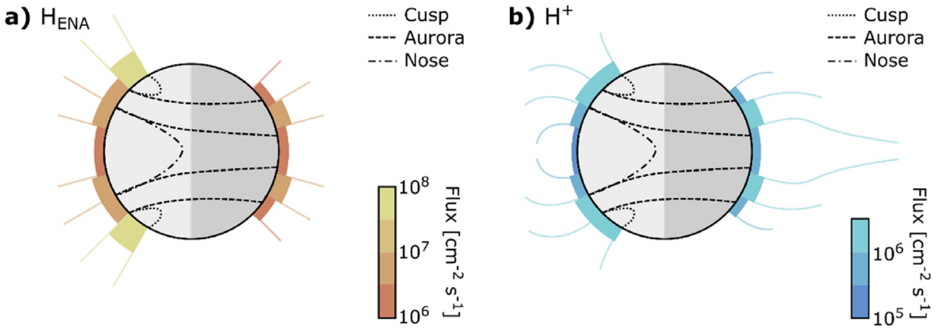

Fig. 4. A schematic illustration of the predicted hydrogen ENA (a) and proton (b) scattering off the Hermean surface. The dashed and dotted lines outline regions corresponding to different classes of plasma precipitation. The direction to the Sun is to the left in the figure. The colored bars represent quantitative estimates of the scattered flux from the surface at different latitudes along the Noon/Midnight meridian. The colored lines emphasize that the scattered protons are guided by the Hermean magnetosphere, while scattered ENAs travel on nearly straight trajectories. (For interpretation of the references to color in this figure legend, the reader is referred to the web version of this article.)

tates the use of models that account for the plasma velocity distribution, to derive the characteristics of the scattered particles.

In Fig. 4, we illustrate the geographical distribution of the expected scattering of hydrogen ENAs and protons, based on the selected precipitation values from Fig. 1 listed in Table 1, together with precipitation maps by Kallio and Janhunen (2003), and the reflection rates from Fig. 3. In Fig. 4, the ENA scattering peaks at the cusps, while protons are scattered at higher fluxes in the auroral regions due to the high impact speeds. Note that these results only apply to the specific precipitation parameters chosen herein, which in reality vary within wide parameter ranges, not necessarily maintaining the proportional relationships between different regions. In this section, we first discuss the model estimates, and then the implications of this scattering for the Hermean ENA- and plasma environments, and the capacity to observe these phenomena.

5.1. Applicability of the lunar empirical models

In the proton scattering (see Cases I and II; the signal in Case III is below the noise level), we note disagreements between the modeled and observed proton scattering rates and spectra. While Case II shows a good qualitative agreement in the spectral shape, there is a quantitative difference of a factor $\sim$2–3. In Case I, there is a quantitative and qualitative disagreement. These disagreements are present despite the fact that the proton scattering models were developed from a data set that included those cases (Lue et al., 2014). This reflects the uncertainty of the observations and the empirical models. In Fig. 4 from Lue et al. (2014), we see that the data scatters with a factor of $\sim$10 in the low solar wind speed observations, and a factor of $\sim$3 in the better constrained high solar wind speed observations. There is likely also a systematic effect that makes the model underestimate the proton backscattering: Lue et al. (2014) excluded the energy bins above the solar wind bulk energy, to avoid an instrumental solar wind cross-talk signal. Although it is unreasonable for backscattered particles to have a higher energy than the incident solar wind, the finite energy bin width as well as the thermal spread of the solar wind distribution means that a significant fraction of the backscattered proton distribution is excluded with the earlier method. From Fig. 2, this underestimation appears to be a factor 3. Thus, although we maintain the use of this model, we note that the proton scattering rate may have uncertainties of a factor of $\lesssim$10. Recent observations by ARTEMIS (Lue et al., 2016b) have also suggested a weaker impact speed-dependence than the model by Lue et al. (2014). However, further study is required to refine the proton scattering models.

It should further be noted that the energy ranges of SWIM and CENA on Chandrayaan-1 are up to $\sim$3 keV/q, and the empirical models have not been validated for higher energies ($>$ 3 keV). The results of the aurora-type precipitation (Fig. 3b), with a very high proton scattering rate (11%), illustrate that the used scattering models may need to be adjusted in the case of very high impact speeds. If the scattered protons and hydrogen atoms are from the same parent distribution, one may expect that the ENA scattering rate should decrease according to the increase of the proton scattering rate at high impact speeds. Such a trend could explain the dependence of the ENA scattering rate with an increased solar wind speed observed by Funsten et al. (2013). The scattering at high impact speeds and the high energy range in the scattered spectra should be addressed by future studies.

In addition to the statistical uncertainties discussed above, it is natural to consider that the difference in regolith properties between the Moon and Mercury may affect the scattering characteristics (the scattering function, energy spectrum, and charge states of the scattered particles). Hermean regolith grains are expected to be similar to the lunar grains regarding the composition (they consist of feldspar and olivine, with nano-phase iron). However, the Hermean regolith also has properties that are different to the lunar regolith. For example, the average grain size is thought to be about half that of the lunar grains (Warell and Blewett, 2004), and the Hermean regolith may be smoother than the lunar regolith (e.g., Warell, 2004). In the present study, we assume no significant change of the scattering characteristics due to these differences. This assumption is supported by lunar observations: no correlations with surface properties have been identified at the Moon, for example between Mare and Highland regions (*e.g.*, Allegrini et al., 2013; Vorburger et al., 2013; 2015; Lue et al., 2016a).

5.2. Scattered hydrogen as a component of Mercury's radiance of energetic neutral atoms

The directional fluxes of scattered hydrogen ENAs predicted herein ($\sim10^7$–10^9 cm^{-2} s^{-1} sr^{-1}) are large in comparison to other ENA sources at Mercury. We will briefly review estimates of other ENA sources below, but we also note that this initial statement is reasonable considering that lunar observations showed solar wind scattering rates of $\sim$10%–20% (McComas et al., 2009; Wieser et al., 2009) and sputtering yields of $\sim$5% (Vorburger et al., 2014) (note that the quantitative comparison depends on the definition of ENAs because of the generally lower energies of sputtered particles). Estimates of sputtered and exospheric charge-exchange ENA populations at Mercury were made by e.g., Lukyanov et al. (2004) and Mura et al. (2005). See also reviews by Orsini et al. (2010) and Saito et al. (2010). Ip (1993) discussed sodium ions (Na^+), photoionized from the Hermean exosphere, which reach high energies in the tail and return to impact the surface, causing sputtering of surface materials. They modeled Na^+ ions from <1 keV to >10 keV. These ions have undergone similar processes as the 'auroral' H^+ that we have discussed herein. Lukyanov et al. (2004) compared the expected sputtered ENA fluxes for three different incident ion populations: cusp H^+ at 1 keV, auroral H^+ at >10 keV, and 1 keV Na^+ ions. The resulting fluxes of sputtered Na ENAs at >100 eV were $9{\cdot}10^5$, $3{\cdot}10^3$, and $9{\cdot}10^3$ cm^{-2} s^{-1} sr^{-1} for the three different sputtering agents respectively. They also discussed ENAs from exospheric charge-exchange, finding values of $\sim10^3$–10^5 cm^{-2} sr^{-1} s^{-1} keV^{-1} for 10–50 keV ENAs. Mura et al. (2005) focused on sputtering from cusp-precipitating H^+ and charge-exchange of the same H^+ population with exospheric neutrals. They discussed sputtered O and Na. They found O ENA fluxes up to 10^8 cm^{-2} s^{-1}, and Na ENA fluxes up to 10^6 cm^{-2} s^{-1}, sputtered from the surface at the cusp. H ENAs generated by charge-exchange were modeled at fluxes of up to 10^5–10^6 cm^{-2} s^{-1} sr^{-1}, radiating tailward from the cusp exosphere at 1–10 keV, and 10^4–10^5 cm^{-2} s^{-1} sr^{-1} at 100 eV–1 keV. These fluxes could also be seen from the sub-solar region at up to 10^5 cm^{-2} s^{-1} sr^{-1}.

Scattered hydrogen ENA remote-sensing will enable imaging of the proton precipitation onto Mercury. The population can be distinguished from other ENA populations using the characteristic shape of the energy spectrum, or mass discrimination (*e.g.*, Vorburger et al., 2014), and the energy spectrum will contain information on both the speed and temperature of the impinging ions (Futaana et al., 2012; 2013; Lue et al., 2016a). Combined investigations of the sputtered and scattered ENAs will add significant value to the study of the Hermean plasma environment. Future ENA observations at Mercury, together with in-situ, simultaneous plasma measurements will provide excellent data for validation of magnetospheric models, and the observations will allow us to follow the dynamics of the Hermean magnetosphere in the variable solar wind environment (Milillo et al., 2010).

5.3. Scattered protons as a component of the Hermean plasma environment

The scattered protons can attain a different pitch-angle distribution compared to the mirroring protons in the Hermean magnetic field. The scattering angle of each scattered particle follows a stochastic process. This is in contrast to mirroring protons, which have a velocity completely perpendicular to the magnetic field at the mirror point. In other words, the surface acts as a strong pitch-angle "scatterer" . An observer at high altitudes will be able to observe upgoing protons within the loss cone, coming on trajectories intersecting the Hermean surface. Raines et al., (2014) and Winslow et al. (2014) observed protons at the Hermean cusp. They observed a clear signature of the loss cone (a decrease in the proton flux in the direction away from the surface, along the magnetic field). Inside the cone, for upgoing directions, the measured fluxes were at $\sim3{\cdot}10^5$ cm^{-2} sr^{-1} s^{-1} (Raines et al., 2014, fig. 6a), which indeed is comparable to the simulated H^+ flux emitted from the cusp surface (integrating Fig. 3a gives $\sim2{\cdot}10^5$ cm^{-2} sr^{-1} s^{-1}). The scattered protons could be one explanation for these upgoing protons in the loss cone.

Protons emitted on closed field lines will likely return to the surface on the other hemisphere, while protons on open field lines can escape through the cusp and mantle, possibly following similar dynamics as O^+ ions in the terrestrial cusp (e.g., Slapak et al., 2013). Trávníček et al. (2007) simulated the dynamics of a proton population emitted isotropically and uniformly from the Hermean surface, though at low energies. These protons either became trapped on closed field lines or escaped both downstream via the cusp, mantle, and tail, and upstream into the foreshock region. More energetic protons from the scattering process would be more capable to escape Mercury but trapping in closed field line regions would also occur, and they may be a significant part of the observed quasi-trapped particle belt around Mercury (Schriver et al., 2011).

Future proton-kinetic computer simulations of the Hermean magnetosphere may shed further light on the dynamics and influence of scattered protons on the Hermean environment. Such simulations could use lunar scattering models to inject scattered protons from the surface into the magnetosphere. Proton circulation, waves, and current systems would be interesting targets for such simulations.

5.4. ENA measurements on Bepicolombo

ENA sensors capable of measuring in the 10 s of eV to a few keV energy range will be carried to Mercury with BepiColombo, a European-Japanese joint mission to Mercury. BepiColombo will be launched in early 2017. BepiColombo is composed of two satellites: Mercury Planetary Orbiter (MPO) and Mercury Magnetospheric Orbiter (MMO). Each spacecraft is equipped with an ENA sensor: The Energetic Neutrals Analyzer, of the Mercury Plasma Particle Experiment (MPPE/ENA) on MMO (Saito et al., 2010a) and the SERENA/ELENA on MPO (Orsini et al., 2010). In particular, MPPE/ENA is an updated version of the CENA sensor used herein and it has equivalent capabilities as CENA, and can therefore address the plasma-surface interaction at Mercury in a similar way as CENA has done at the Moon. The extrapolated predictions made in the present study will be used for interpreting the data obtained by MPPE/ENA. The expected differential fluxes of ENAs at Mercury are very similar to those observed at the Moon.

6. Concluding remarks

The Moon is a natural laboratory for the study of particle interactions with regolith. The lessons learned at the Moon can be applied to better understand ongoing and future measurements at other airless planetary objects. The variable plasma environment at the Moon, and the variation in its surface properties allow us to span a large parameter space for scattering models. Nevertheless, future comparative studies between different airless bodies, in different plasma environments, are likely to reveal further details which will add to our understanding of the scattering process, its role in planetary environments, and its applications as a remote-sensing tool.

Acknowledgments

The authors thank K. W. Ogilvie (NASA/GSFC) and A. J. Lazarus (MIT) for providing Wind/SWE data via the MIT Space Plasma Group (http://web.mit.edu/space/www/). We also thank Y. Saito (JAXA/ISAS) and M. Nishino (Nagoya University) for providing Kaguya/MAP-PACE data, also available at the Kaguya Data Archive (http://l2db.selene.darts.isas.jaxa.jp/index.html.en). The Chandrayaan-1/SARA data are available at the Indian Space Science Data Center (ISSDC, http://www.issdc.gov.in/chandrayaan1.html). This work was supported by the Swedish National Space Board (SNSB) (Dnr:97/11) and NASA (Grant NNX15AP89G). The work has benefited from collaboration enabled by the JSPS (Japan Society for the Promotion of Science) Summer Program 2014 and ISSI (International Space Science Institute) International Team 336.

References

Allegrini, F., et al., 2013. Lunar energetic neutral atom (ENA) spectra measured by the interstellar boundary explorer (IBEX). Planet. Space Sci. 85, 232–242. doi:10.1016/j.pss.2013.06.014.

Anderson, B.J., et al., 2011. The global magnetic field of Mercury from MESSENGER orbital observations. Science 333 (6051), 1859–1862. doi:10.1126/science.1211001.

Asbridge, J.R., Bame, S.J., Strong, I.B., 1968. Outward flow of protons from the Earth's bow shock. J. Geophys. Res. 73 (17), 5777–5782. doi:10.1029/JA073i017p05777.

Baker, D.N., et al., 2011. The space environment of Mercury at the times of the second and third MESSENGER flybys. Planet. Space Sci. 59 (15), 2066–2074. doi:10.1016/j.pss/2011.01.018.

Barabash, S., et al., 2009. Investigation of the solar wind-Moon interaction onboard Chandrayaan-1 mission with the SARA experiment. Curr. Sci. 96 (4), 526–532.

DiBraccio, G.A., et al., 2015. First observations of Mercury's plasma mantle by MESSENGER. Geophys. Res. Lett. 42. doi:10.1002/2015GL065805.

Feldman, W.C., Asbridge, J.R., Bame, S.J., Gosling, J.T., 1978. Long-term variations of selected solar wind properties: imp 6, 7, and 8 results. J. Geophys. Res. 83 (A5), 2177–2189. doi:10.1029/JA083iA05p02177.

Formisano, V., Moreno, G., Palmiotto, F., Hedgecock, P.C., 1973. Solar wind interaction with the Earth's magnetic field 1. Magnetosheath. J. Geophys. Res. 78 (19), 3714–3730. doi:10.1029/JA078i019p03714.

Frank, L.A., 1985. Plasmas in the earth's magnetotail. Space Sci. Rev 42 (1), 211–240. doi:10.1007/BF00218233.

Funsten, H.O., et al., 2013. Reflection of solar wind hydrogen from the lunar surface. J. Geophys. Res. Planets 118, 293–305. doi:10.1002/jgre.20055.

Futaana, Y., Barabash, S., Holmström, M., Bhardwaj, A., 2006. Low energy neutral atoms imaging of the Moon. Planet. Space Sci. 54 (2), 132–143. doi:10.1016/j.pss.2005.10.010.

Futaana, Y., Barabash, S., Wieser, M., Holmström, M., Lue, C., Wurz, P., Schaufelberger, A., Bhardwaj, A., Dhanya, M.B., Asamura, K., 2012. Empirical energy spectra of neutralized solar wind protons from the lunar regolith. J. Geophys. Res. 117, E05005. doi:10.1029/2011JE004019.

Futaana, Y., Barabash, S., Wieser, M., Lue, C., Wurz, P., Vorburger, A., Bhardwaj, A., Asamura, K., 2013. Remote energetic neutral atom imaging of electric potential over a lunar magnetic anomaly. Geophys. Res. Lett. 40 (2), 262–266. doi:10.1002/grl.50135.

Gershman, D.J., Slavin, J.A., Raines, J.M., Zurbuchen, T.H., Anderson, B.J., Korth, H., Baker, D.N., Solomon, S.C., 2013. Magnetic flux pileup and plasma depletion in Mercury's subsolar magnetosheath. J. Geophys. Res. 118, 7181–7199. doi:10.1002/2013JA019244.

Goldstein, B.E., Suess, S.T., Walker, R.J., 1981. Mercury: Magnetospheric processes and the atmospheric supply and loss rates. J. Geophys. Res. 86 (A7), 5485–5499. doi:10.1029/JA086iA07o05485.

Grande, M., 1997. Investigation of magnetospheric interactions with the Hermean surface. Adv. Space Res. 19 (10), 1609–1614. doi:10.1016/S0273-1177(97)00374-8.

Hapke, B., 2001. Space weathering from Mercury to the Asteroid belt. J. Geophys. Res. 106 (E5), 10039–10073. doi:10.1029/2000JE001338.

Imber, S.M., Slavin, J.A., Boardsen, S.A., Anderson, B.J., Korth, H., McNutt Jr., R.L., Solomon, S.C., 2014. MESSENGER observations of large dayside flux transfer events: do they drive Mercury's substorm cycle? J. Geophys. Res. 119, 5613–5623. doi:10.1002/2014JA019884.

Ip, W.-H., 1993. On the surface sputtering effects of magnetospheric charged particles at Mercury. Astrophys. J. 418, 451–456. doi:10.1029/1993ApJ...418..451I.

Johnson, R.E., Baragiola, R., 1991. Lunar surface: Sputtering and secondary ion mass spectrometry. Geophys. Res. Lett. 18 (11), 2169–2172. doi:10.1029/91GL02095.

Kabin, T., Gombosi, T.I., DeZeeuw, D.L., Powell, K.G., 2000. Interaction of Mercury with the Solar Wind. Icarus 143 (2), 397–406. doi:10.1006/icar.1999.6252.

Kallio, E., Janhunen, P., 2003. Solar wind and magnetospheric ion impact on Mercury's surface. Geophys. Res. Lett. 30 (17), 1877. doi:10.1029/2003GL017842.

Katsavrias, C., Preka-Papadema, P., Moussas, X., 2012. Wavelet analysis on solar wind parameters and geomagnetic indices. Sol. Phys. 280, 623. doi:10.1007/s11207-012-0078-6.

Kazama, Y., Barabash, S., Bhardwaj, A., Asamura, K., Futaana, Y., Holmström, M., Lundin, R., Sridharan, R., Wurz, P., 2006. Energetic neutral atom imaging mass spectroscopy of the Moon and Mercury environments. Adv. Space Res 37, 38–44. doi:10.10169/j.asr.2005.05.047.

Killen, R.M., Ip, W.-H., 1999. The surface-bounded atmospheres of Mercury and the Moon. Rev. Geophys 37 (3), 361–406. doi:10.1029/1999RG900001.

Killen, R., et al., 2007. Processes that promote and deplete the exosphere of Mercury. Space Sci. Rev. 132, 433–509. doi:10.1007/s11214-007-9232-0.

Leblanc, F., Luhmann, J.G., Johnson, R.E., Liu, M., 2003. Solar energetic particle event at Mercury. Planet. Space Sci. 51, 339–352. doi:10.1016/S0032-0633(02)00207-6.

Lopez, R.E., Freeman, J.W., 1986. Solar wind proton temperature-velocity relationship. J. Geophys. Res. 91 (A2), 1701–1705. doi:10.1029/JA091iA02p01701.

Lue, C., Futaana, Y., Barabash, S., Wieser, M., Holmström, M., Bhardwaj, A., Dhanya, M.B., Wurz, P., 2011. Strong influence of lunar crustal fields on the solar wind flow. Geophys. Res. Lett. 38, L03202. doi:10.1029/2010GL046215.

Lue, C., Futaana, Y., Barabash, S., Wieser, M., Bhardwaj, A., Wurz, P., 2014. Chandrayaan-1 observations of backscattered solar wind protons from the lunar regolith: dependence on the solar wind speed. J. Geophys. Res. Planets 119, 968–975. doi:10.1002/2013JE004582.

Lue, C., Futaana, Y., Barabash, S., Saito, Y., Nishino, M., Wieser, M., Asamura, K., Bhardwaj, A., Wurz, P., 2016a. Scattering characteristics and imaging of energetic neutral atoms from the Moon in the terrestrial magnetosheath. J. Geophys. Res. doi:10.1002/2015JA021826.

Lue, M.C., Halekas, J.S., Poppe, A.R., McFadden, J.P., 2016b. ARTEMIS observations of proton scattering off the lunar surface. Fall Meeting Abstracts. American Geophysical Union.

Lukyanov, A., Barabash, S., Holmström, M., 2004. Energetic neutral atom imaging at Mercury. Adv. Space Res. 33 (11), 1890–1898. doi:10.1016/j.asr.2003.05.035.

Marsch, E., Mühlhäuser, K.-H., Schwenn, R., Rosenbauer, H., Pilipp, W., Neubauer, F.M., 1982. Solar wind protons: three-dimensional velocity distributions and derived plasma parameters measured between 0.3 and 1 AU. J. Geophys. Res. 87 (A1), 52–72. doi:10.1029/JA087iA01p00052.

Massetti, S., Orsini, S., Milillo, A., Mura, A., De Angelis, E., Lammer, H., Wurz, P., 2003. Mapping of the cusp plasma precipitation on the surface of Mercury. Icarus 166, 229–237. doi:10.1016/j.icarus.2003.08.005.

McCann, D., Barabash, S., Nilsson, H., Bhardwaj, A., 2007. Miniature ion mass analyzer. Planet. Space Sci. 55 (9), 1190–1196. doi:10.1016/j.pss.2006.11.020.

McComas, D.J., et al., 2009. Lunar backscatter and neutralization of the solar wind: First observations of neutral atoms from the Moon. Geophys. Res. Lett. 36, L12104. doi:10.1029/2009GL038794.

Milillo, A., Wurz, P., Orsini, S., Delcourt, D., Kallio, E., Killen, R.M., Lammer, H., Massetti, S., Mura, A., Barabash, S., et al., 2005. Surface-exosphere-magnetosphere system of Mercury. Space Sci. Rev. 117, 397–443. doi:10.1007/s11214-005-3593-z.

Milillo, A., et al., 2010. The BepiColombo mission: an outstanding too for investigating the Hermean environment. Planet. Space Sci. 58 (1–2), 40–60. doi:10.1016/j.pss.2008.06.005.

Mura, A., Orsini, S., Milillo, A., Delcourt, D., Massetti, S., De Angelis, E., 2005. Dayside H+ circulation at Mercury and neutral particle emission. Icarus 175, 305–319. doi:10.1016/j.icarus.2004.12.010.

Ness, N.F., Behannon, K.W., Lepping, R.P., Wang, Y.C., 1975. The magnetic field of Mercury, 1. J. Geophys. Res. 80 (19), 2708–2716. doi:10.1029/JA080i019p02708.

Niehus, H., Heiland, W., Taglauer, E., 1993. Low-energy ion scattering at surfaces. Surf. Sci. Rep. 17 (4–5), 213–303. doi:10.1016/0167-5729(93)90024-J.

Ogilvie, K.W., et al., 1995. SWE, a comprehensive plasma instrument for the WIND spacecraft. Space Sci. Rev. 71 (1), 55–77. doi:10.1007/BF00751326.

Orsini, S., Livi, S., Torkar, K., Barabash, S., Milillo, A., Wurz, P., Di Lellis, A.M., Kallio, E.the SERENA team, 2010. SERENA: A suite of four instruments (ELENA, STROFIO, PICAM, and MIPA) on board BepiColombo-MPO for particle detection in the Hermean evironment. Planet. Space Sci. 58, 166–181. doi:10.1016/j.pss.2008.09.012.

Parker, E.N., 1958. Dynamivs of the interplanetary gas and magnetic fields. Astrophys. J. 128, 664–676. doi:10.1086/146579.

Pieters, C.M., et al., 2009. Character and spatial distribution of OH/H2O on the surface of the Moon seen by M3 on Chandrayaan-1. Science 326 (5952), 568–572. doi:10.1126/science.1178658.

Poh, G., et al., 2016. MESSENGER observations of cusp plasma filaments at Mercury. J. Geophys. Res. 121, 8260–8285. doi:10.1002/2016JA022552.

Poppe, A.R., Sarantos, M., Halekas, J.S., Delory, G.T., Saito, Y., Nishino, M., 2014. Anisotropic solar wind sputtering of the lunar surface induced by crustal magnetic anomalies. Geophys. Res. Lett. 41 (14), 4865–4872. doi:10.1002/2014GL060523.

Raines, J.M., et al., 2013. Distribution and compositional variations of plasma ions in Mercury's space environment: the first three Mercury years of MESSENGER observations. J. Geophys. Res. 118, 1604–1619. doi:10.1029/2012JA018073.

Raines, J.M., Gershman, D.J., Slavin, J.A., Zurbuchen, T.H., Korth, H., Anderson, B.J., Solomon, S.C., 2014. Structure and dynamics of Mercury's magnetospheric cusp: MESSENGER measurements of protons and planetary ions. J. Geophys. Res. 119 (8), 6587–6602. doi:10.1002/2014JA020120.

Raines, J.M., et al., 2015. Plasma sources in planetary magnetospheres: Mercury. Space Sci. Rev., 192 (1), 91–144. doi:10.1007/s11214-015-0193-4.

Rodríguez, M.D.F., Saul, L., Wurz, P., Fuselier, S.A., McComas, D.J., Möbius, E., 2012. IBEX-Lo observations of energetic neutral hydrogen atoms originating from the lunar surface. Planet. Space Sci. 60 (1), 297–303. doi:10.1016/j.pss.2011.09.009.

Saito, Y., et al., 2008. Solar wind proton reflection at the lunar surface: low energy ion measurement by MAP-PACE onboard SELENE(KAGUYA). Geophys. Res. Lett. 35, L24205. doi:10.1029/2008GL036077.

Saito, Y., et al., 2012. Simultaneous observation of the electron acceleration and ion deceleration over lunar magnetic anomalies. Earth, Planets and Space 64 (4). doi:10.5047/eps.2011.07.011.

Saito, Y., Sauvaud, J.A., Hirahara, M., Barabash, S., Delcourt, D., Takahashima, T., Asamura, K.BepiColombo MMO/MPPE team, 2010a. Scientific objectives and instrumentation of Mercury Plasma Particle Experiment (MPPE) onboard MMO. Planet. Space Sci. 58, 182–200. doi:10.1016/j.pss.2008.06.003.

Saito, Y., et al., 2010b. In-flight performance and initial results of plasma energy angle and composition experiment (PACE) on SELENE (Kaguya). Space Sci. Rev. 154 (1–4), 265–303. doi:10.1007/s11214-010-9647-x.

Sarantos, M., Killen, R.M., Kim, D., 2007. Predicting the long-term solar wind ion-sputtering source at Mercury. Planet. Space Sci, 55, 1584–1595. doi:10.1016/j.pss.2006.10.011.

Schaufelberger, A., et al., 2011. Scattering function for energetic neutral hydrogen atoms off the lunar surface. Geophys. Res. Lett. 38 (22). doi:10.1029/2011GL049362.

Schriver, D., et al., 2011. Quasi-trapped ion and electron populations at Mercury. Geophys. Res. Lett. 38, L23103. doi:10.1029/2011GL049629.

Slapak, R., Nilsson, H., Westerberg, L.G., 2013. A statistical study on O+ flux in the dayside magnetosheath. Ann. Geophys. 31, 1005–1010. doi:10.5194/angeo-31-1005-2013.

Slavin, J.A., et al., 2009. MESSENGER observations of magnetic reconnection in Mercury's magnetosphere. Science 324 (606). doi:10.1126/science.1172011.

Slavin, J.A., et al., 2014. MESSENGER observations of Mercury's dayside magnetosphere under extreme solar wind conditions. J. Geophys. Res. 119, 8087–8116. doi:10.1002/2014JA020319.

Sun, W.J., Fu, S.Y., Slavin, J.A., Raines, J.M., Zong, Q.G., Poh, G.K., Zurbuchen, T.H., 2016. Spatial distribution of Mercury's flux ropes and reconnection fronts: MESSENGER observations. J. Geophys. Res. 121, 7590–7607. doi:10.1002/2016JA022787.

Trávníček, P., Hellinger, P., Schriver, D., 2007. Structure of Mercury's magnetosphere for different pressure of the solar wind: three dimensional hybrid simulations. Geophys. Res. Lett. 34, L05104. doi:10.1029/2006GL028518.

Vorburger, A., Wurz, P., Barabash, S., Wieser, M., Futaana, Y., Holmström, M., Bhardwaj, A., Asamura, K., 2012. Energetic neutral atom observations of magnetic anomalies on the lunar surface. J. Geophys. Res. 117, A07208. doi:10.1029/2012JA017553.

Vorburger, A., Wurz, P., Barabash, S., Wieser, M., Futaana, Y., Lue, C., Holmström, M., Bhardwaj, A., Dhanya, M.B., Asamura, K., 2013. Energetic neutral atom imaging of the lunar surface. J. Geophys. Res. 118, 3937–3945. doi:10.1002/jgra.50337.

Vorburger, A., Wurz, P., Barabash, S., Wieser, M., Futaana, Y., Holmström, M., Bhardwaj, A., Asamura, K., 2014. First direct observation of sputtered lunar oxygen. J. Geophys. Res. 119, 709–722. doi:10.1002/2013JA019207.

Vorburger, A., Wurz, P., Barabash, S., Wieser, M., Futaana, Y., Bhardwaj, A., Asamura, K., 2015. Imaging the South Pole-Aitken basin in backscattered neutral hydrogen atoms. Planet. Space Sci. 115, 57–63. doi:10.1016/j.pss.2015.02.007.

Warell, J., 2004. Properties of the Hermean regolith: IV. Photometric parameters of Mercury and the Moon contrasted with Hapke modelling. Icarus 167 (2), 271–286. doi:10.1016/j.icarus.2003.10.010.

Warell, J., Blewett, D.T., 2004. Properties of the Hermean regolith: V. New optical reflectance spectra, comparison with lunar anorthosites, and mineralogical modelling. Icarus 168 (2), 257–276. doi:10.1016/j.icarus.2003.10.020.

Wieser, M., Barabash, S., Futaana, Y., Holmström, M., Bhardwaj, A., Sridharan, R., Dhanya, M.B., Wurz, P., Schaufelberger, A., Asamura, K., 2009. Extremely high reflection of solar wind protons as neutral hydrogen atoms from regolith in space. Planet. Space Sci. 57 (14–15), 2132–2134. doi:10.1016/j.pss.2009.09.012.

Wieser, M., Barabash, S., Futaana, Y., Holmström, M., Bhardwaj, A., Sridharan, R., Dhanya, M.B., Schaufelberger, A., Wurz, P., Asamura, K., 2010. First observation of a mini-magnetosphere above a lunar magnetic anomaly using energetic neutral atoms. Geophys. Res. Lett. 37, L05103. doi:10.1029/2009GL041721.

Winslow, R.M., et al., 2014. Mercury's surface magnetic field determined from proton-reflection magnetrometry. Geophys. Res. Lett. 41, 4463–4470. doi:10.1002/2014GL060258.

Wurz, P., 2000. Detection of energetic neutral particles. In: Scherer, K., Fichtner, H., Marsch, E. (Eds.), The Outer Heliosphere: Beyond the Planets. Copernicus Gesellschaft e. V, Katlenburg- Lindau, pp. 251–288.